Research Article Vol. 9, No. 8 / August 2022 / Optica 953

OPTICA

On-chip spin-orbit locking of quantum emitters in 2D materials for chiral emission

Yichen Ma,[1,2,†] Haoqi Zhao,[3,†] Na Liu,[1,2] Zihe Gao,[4] Seyed Sepehr Mohajerani,[1,2] Licheng Xiao,[1,2] James Hone,[5] Liang Feng,[3,4,6] and Stefan Strauf[1,7]

[1]Department of Physics, Stevens Institute of Technology, Hoboken, New Jersey 07030, USA
[2]Center for Quantum Science and Engineering, Stevens Institute of Technology, Hoboken, New Jersey 07030, USA
[3]Department of Electrical and Systems Engineering, University of Pennsylvania, Philadelphia, Pennsylvania 19104, USA
[4]Department of Materials Science and Engineering, University of Pennsylvania, Philadelphia, Pennsylvania 19104, USA
[5]Department of Mechanical Engineering, Columbia University, New York, New York 10027, USA
[6]e-mail: fenglia@seas.upenn.edu
[7]e-mail: strauf@stevens.edu

Received 9 May 2022; revised 12 July 2022; accepted 14 July 2022; published 18 August 2022

Light carries both spin angular momentum (SAM) and orbital angular momentum (OAM), which can be used as potential degrees of freedom for quantum information processing. Quantum emitters are ideal candidates towards on-chip control and manipulation of the full SAM–OAM state space. Here, we show coupling of a spin-polarized quantum emitter in a monolayer WSe_2 with the whispering gallery mode of a Si_3N_4 ring resonator. The cavity mode carries a transverse SAM of $\sigma = \pm 1$ in the evanescent regions, with the sign depending on the orbital power flow direction of the light. By tailoring the cavity–emitter interaction, we couple the intrinsic spin state of the quantum emitter to the SAM and propagation direction of the cavity mode, which leads to spin–orbit locking and subsequent chiral single-photon emission. Furthermore, by engineering how light is scattered from the WGM, we create a high-order Bessel beam which opens up the possibility to generate optical vortex carrying OAM states.

https://doi.org/10.1364/OPTICA.463481

1. INTRODUCTION

Quantum technologies have revolutionized the basic form of information processing, in which quantum states are used to encode information for communication between qubits [1]. The photonic approach to quantum information is to use photons as qubits and achieve exchange of information via light–matter interaction. Further advances in quantum technologies demands miniaturization of the device, robust system integration, and a more controlled light–matter interaction, which leads to the advent of on-chip quantum photonic circuits [2]. Chirality is a fundamental feature in myriad physical systems. There are two degrees of freedom to characterize the chiral nature of light: the spin angular momentum (SAM) of light, which is determined by the polarization degree of freedom, and the orbital angular momentum (OAM), which is related to the spatial degree of freedom [3,4]. Their respective couplings in the form of spin–orbit interaction (SOI) leads to many striking applications such as observation of the spin-Hall effect [5–9], generation of optical vortex carrying OAM states [10–14] and spin-direction locking at the evanescent fields [15–19]. The chirality that arises from the spin-direction locking effects in nanophotonic waveguides adds new functionality to on-chip devices. Due to the strong lateral confinement inside the waveguide, light propagating at the evanescent regions will have a $\pm\pi/2$ phase difference between the longitudinal and transverse components, which leads to clockwise (CW) and counterclockwise (CCW) circularly polarized light, with the polarization state depending on the propagation direction of the light. This spin-direction coupling behavior defines the chirality of the waveguide modes and can be incorporated to a whispering gallery mode (WGM)-based ring resonator with angular scatterers to further control the SOI phenomena in the full SAM–OAM space [14,20].

While the preceding examples focus on tailoring classical light, recent progress demonstrates that either OAM or SAM control can also be conveniently conducted at the single-quanta level, making it now also a robust system for quantum applications taking full advantage of chiral degrees of freedom of photons [21,22]. Particularly, a superposition of single-photon OAM states has been achieved by Chen *et al.* [21] by integration of semiconductor quantum dots to ring resonators with angular gratings, which opens the possibility for high-dimensional quantum information processing. Likewise, Coles *et al.* [22] showed that spin-polarized quantum dots coupled to linear waveguides generate chiral single-photon emission. If one can further integrate the spin-orbit locking effect onto the generation of OAM states and lift the spin degeneracy of the quantum emitter, the superposition of many OAM states can transform into a well-defined single-OAM state.

Full control of the SAM–OAM space of a single photon can be achieved if one can couple spin-polarized quantum emitter to

spin–orbit locking WGM-based ring resonator. To this end, strain-induced quantum emitters in monolayer WSe_2 have emerged as a promising candidate for on-chip integration. Coupling effects between the 2D excitons in monolayer WSe_2 and WGM mode resonators have already been demonstrated via the evanescent field coupling [23,24]. The transition from 2D excitons into 0D quantum emitters requires only a localized strain potential to confine the carriers, which can be engineered to be spatially deterministic [25–27]. Particularly, the strain-induced emitters created by transferring monolayer WSe_2 onto a waveguide are located exactly at the evanescent regions [28], which significantly reduces the fabrication complexity for such a system. In addition, the quantum emitters in WSe_2 possess an intrinsic degree of freedom, which is related to the valley pseudospin vectors at the $\pm$ K points of the Brillouin zone [29]. By applying an external magnetic field, this degeneracy can be lifted via the Zeeman effect to create spin-polarized single photons. Owing to the large g-factor of strain-induced quantum emitters in WSe_2, which are typically 6–10 [30], these quantum emitters can be spectrally tuned into resonance with the cavity mode by adjusting the magnetic field.

Here, we demonstrate creation of chiral single-photon emission by coupling strain-induced quantum emitters in monolayer WSe_2 to the WGM of a Si_3N_4 ring resonator. The quantum emitters are created over the edge of the ring resonator, which inherently couples the spin-locking mode of the ring resonator via the evanescent field. We fully investigate the cavity-emitter coupling effects and characterize the Purcell-enhanced optical emission. Through circular polarization-resolved imaging measurements, we observe opposite spin states associated with the emission from the quantum emitter and ring resonator, which confirm the interaction between the spin state of the quantum emitter and the spin-dependent chirality of the cavity mode. We further demonstrate that the emitted light is a Bessel beam due to the spherical symmetry of the WGM and angular gratings.

2. RESULTS

To illustrate the physics behind the spin-orbit locking behavior of the WGM, we perform finite-difference time-domain (FDTD) simulations of the fundamental TE mode of the Si_3N_4 ring resonator on a SiO_2 substrate. Figure 1(a) shows the cross-section view of the transverse electric field intensity map E_{trans}. The black arrow illustrates the oscillation direction of the electric field and the dashed rectangle indicates the dimension of the ring resonator cross-section, which has a height of 220 nm and width of 500 nm. The strong confinement of light inside the ring resonator leads to an evanescent field at both sidewalls, with the right (outer) sidewall field being more extended due to the bending of the ring. In this evanescent region, a local longitudinal field E_{long} can be observed with a $\pm\pi/2$ phase difference to the transverse field, as shown in Fig. 1(b). (See Supplement 1, Section S1 for details of the FDTD simulations.) The phase difference is expressed as the imaginary unit multiplier with an opposite sign on the inner and outer sidewalls. The ratio between the longitudinal component and the transverse component iE_{long}/E_{trans} determines the transverse SAM, which is perpendicular to the propagation plane [31]. By engineering the geometry of the ring resonator, this ratio can be near unity at the evanescent region outside the sidewall [Fig. 1(c)], resulting in a high purity transverse spin state $\sigma\pm$ at these regions with $\sigma_+ = \frac{1}{\sqrt{2}}(E_{tran} + iE_{long})$ and $\sigma_- = \frac{1}{\sqrt{2}}(E_{tran} - iE_{long})$. In the propagation plane, this is simply the right-handed and left-handed circular polarization. Figures 1(d) and 1(e) show the top view of the transverse spin distribution under counterclockwise (CCW) and clockwise (CW) propagation directions, respectively. The inner and outer sidewalls have opposite transverse spin states and their sign flips when the power flow direction inside the cavity reverses, arising from the designed spin-orbit locking nature of the WGM in the evanescent regions described previously. As a result, given a spin-polarized quantum emitter is located at the outer sidewall, it can only couple to one unidirectional WGM if the emitter is spectrally on resonance.

The creation of strain-induced quantum emitters in monolayer WSe_2 perfectly meets the requirement to place the quantum emitter at the sidewall of the ring resonator. Specifically, the edges of the ring resonator provide a height difference to activate the strain field for trapping excitons. To avoid breaking of the monolayer by directly transferring it onto the ring resonator, we intentionally

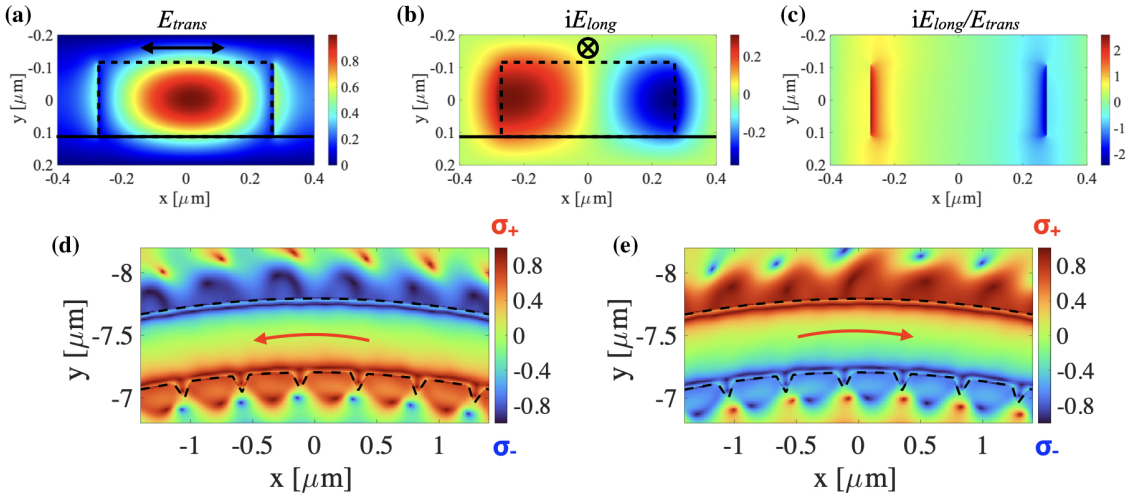

Fig. 1. FDTD simulation of traveling-wave quasi-TE mode. Cross-section distribution of the (a) transverse component and (b) longitudinal component of the electric field. There is a $\pi/2$ phase difference between these two components. (c) Cross-section distribution of electric field component ratio iE_{long}/E_{trans}. The absolute value of this ratio is near unity at the sidewall, implying a pure transverse spin. Top view of the transverse spin distribution of (d) counter-clockwise and (e) clockwise quasi-TE mode. The inner and outer sidewalls have opposite chirality (σ^+ colored red, σ^- colored blue), which changes when the power flow direction (red arrow) reverses, showing a spin–orbit locking phenomenon.

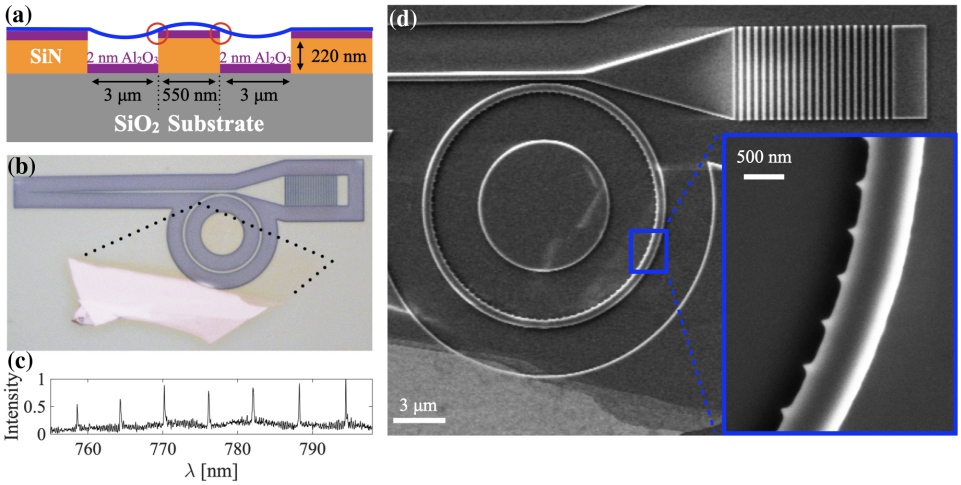

Fig. 2. Device overview. (a) Schematic of the spin–orbit locking device. 220 nm of SiN is deposited on top of a SiO_2/Si substrate. The width of the patterned ring and air trenches are 500 nm and 3 μm, respectively. The red circles illustrate the location of the strain-induced quantum emitters at the inner and outer edge of the ring. (b) Optical image of the ring resonator with adjacent grating coupler. The dry-transferred monolayer of WSe_2 is outlined by the dotted black lines covering about $^3/_4$ of the ring resonator. The attached bulk WSe_2 reveals itself at the bottom of the image due to its high reflectivity but does not overlap with the ring. (c) The measured spectrum of the quasi-TE mode distribution by exciting through the grating coupler. (d) Scanning electron microscope image of the ring resonator with WSe_2 monolayer. The inset shows a zoomed view of the scatterers located at the inner sidewall for a 3 μm long section that matches the simulated area shown in Figs. 1(d) and 1(e).

suspend the monolayer WSe_2 by etching air trenches around the ring resonator core [28]. Figure 2(a) illustrates the schematic of the device. We etched two 3 μm wide trenches on both the inner and outer side of the ring resonator to suspend the monolayer and deposited 2 nm of Al_2O_3 as an insulation layer to prevent spectral diffusion due to interaction with charges trapped inside Si_3N_4 [32]. Details of the fabrication process can be found in Supplement 1, Section S2. The monolayer WSe_2 is mechanically exfoliated from bulk crystal and then dry transferred onto the Si_3N_4 ring resonator, which is evanescently coupled to a single port Si_3N_4 waveguide attached to a grating coupler, as shown in Fig. 2(b). The grating coupler allows us to pump and measure the cavity modes directly using cross-polarization pump and probe detection. The measured spectrum [Fig. 2(c)] shows cavity modes from 750 to 800 nm with an average free spectral range of 6.11 ± 0.3 nm and FWHM of 0.12 ± 0.02 nm, corresponding to an optical quality factor $Q = 6500$. The SEM image [Fig. 2(d)] highlights the periodic scatterers that have been patterned along the inner sidewall of the ring resonator to convert near-field light from the evanescent region into the far-field radiation for efficient light collection.

The photoluminescence (PL) signal is collected by a high NA (0.82) objective located inside a closed-cycle cryogenic system with base temperature of 3.8 K, allowing us to collect light from a solid angle of $\pm 54°$. See Supplement 1, Fig. S3 for a typical PL spectrum of the monolayer WSe_2 as well as a filtered spectrum of a single quantum emitter. By applying an external magnetic field in the Faraday geometry (B||z), one can separate the σ_+ and σ_- components of the exciton emission via the valley Zeeman effect, with an energy splitting given by $\Delta_B = \sqrt{(\Delta_0)^2 + (\mu_B g B)^2}$, where Δ_0 is the zero-field splitting energy, μ_B the Bohr magneton, and g the exciton's g factor [29]. This lifting of the degeneracy in the circularly polarized basis allows us not only to precisely select the chirality of the emitted single photon, but also to effectively tune the emission on and off resonance with the cavity mode. The typical g factor of these strain-induced quantum emitters are $g = 6 - 10$, which leads to a maximal emitter-mode tuning range of about 1.5 nm [30]. Due to the anisotropic strain and thermalization effects, the low-energy peak of the doublet often dominates in the PL spectrum [27,30,33]. Therefore, we focus on studying quantum emitters that are typically 1 nm or less blue detuned from the measured cavity mode at zero magnetic field. Figure 3(a) shows by sweeping the magnetic field from 0T to 9T, we tune the σ_+ branch of the emission into resonance with the measured cavity mode at 7T. The increase of PL intensity at the resonant wavelength shows pronounced coupling between the quantum emitter and the ring resonator, despite the rather large mode volume V_{eff} of these ring resonators. To quantify the coupling strengths, we measure the time-resolved emission from the emitter and extract from the fit a lifetime of $T_{1,off} = 5.2$ ns for the uncoupled case ($B = 0\,T$) and $T_{1,on} = 3.55$ ns for the coupled case ($B = 7\,T$) [Fig. 3(b)]. The calculation of the Purcell factor requires knowledge of the quantum yield of the emitter, which we estimated to be about 15–25% for the strain-induced quantum emitters in the flux-grown WSe_2 [27], yielding an experimental Purcell factor $F_p = 2.8 - 4.1$. This matches well with the theoretically calculated Purcell factor of $F_p = 2.8$ determined from the Q/V ratio formula, as well as $F_p = 2.7$ based on the Jaynes–Cummings model, as further detailed in Supplement 1, Sections S4 and S5. Note that the strain-induced quantum emitters are created in principle at both the inner and outer sidewalls of the cavity. However, the additional scatterers at the inner sidewall push the evanescent field further away from the material edge, such that any strain-induced quantum emitters created at these locations are spatially away from the cavity mode, and thus experience only 30% of the emitter-cavity coupling strength compared to the outer sidewall. A detailed analysis of the coupling strength as a function of the horizontal displacement can be found in Supplement 1, Section S4. Therefore, to observe pronounced coupling of quantum emitters, they must reside at the edge of the outer sidewall of the ring resonator, where they undergo spin–orbit locking, as dictated by the power flow direction in the ring resonator.

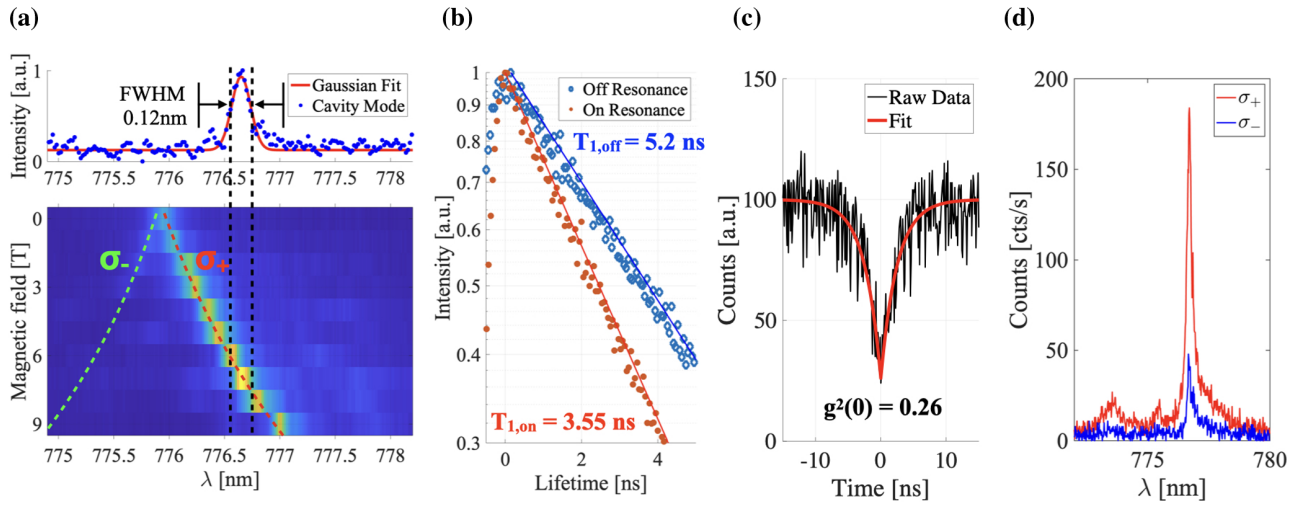

Fig. 3. Cavity-quantum emitter coupling effects (a) Top: Measured cavity resonance mode with a FWHM of 0.12 nm. Bottom: Intensity map of the PL emission spectrum as a function of the magnetic field tuning the σ^+ spin component into resonance. (b) Comparison of measured lifetime with the quantum emitter on- (red) and off-resonance (blue) with the cavity mode. The off-resonance case is recorded at 0T with a detuning energy of $\delta = 1.52$ meV and yields $T_1 = 5.2$ ns. On-resonance, $\delta = 0$ and $T_1 = 3.55$ ns at 7T. (c) Second-order photon correlation histogram recorded under continuous-wave laser excitation (black). Red line is a mono-exponential fit yielding pronounced antibunching with $g^{(2)}(0) = 0.26$. (d) PL spectrum recorded from the quantum emitter position on the ring that is tuned into resonance at 7T and resolved in σ_+ and σ_- polarization contributions. The corresponding polarization degree of 59% is strongly reduced from the initial value of 90% in the uncoupled case due to the underlying spin–orbit locking effect.

To investigate the quantum nature of emitted photons, we use a standard Hanbury–Brown and Twiss detection setup to record the second-order photon correlation function $g^{(2)}(\tau)$, as shown in Fig. 3(c). A mono-exponential fit yields $g^{(2)}(0) = 0.26$, which confirms single-photon emission. It is well understood that the strain-induced quantum emitters in WSe2 possess an intrinsic spin degree of freedom, which can be optically observed as linearly polarized light at zero external magnetic field, and circularly polarized light above approximately 2T [34]. To resolve the circular polarization nature of the emitted single-photon stream, a quarter-wave plate followed by a linear polarizer was placed in the detection path to analyze the σ_+ and σ_- components of the PL spectrum. We first provide an analysis of an uncoupled quantum emitter in a magnetic field and show that two peaks of the doublet can be resolved in σ_+ and σ_- polarization, respectively (see Supplement 1, Section S6). As described previously, we focus on studying the low-energy transition of the doublet because it has the higher oscillator strength since the high-energy component is strongly thermalized at elevated magnetic fields [27,30,33]. One can then define the polarization degree for the dominant low-energy peak as $\chi_{PL} = \frac{I_+ - I_-}{I_+ + I_-}$, where I_+ and I_- stands for the integrated PL intensity under the σ_+ and σ_- detection schemes, respectively. The extracted χ_{PL} for the uncoupled quantum emitter is 90%, which confirms that the lower energy peak is intrinsically σ_+ polarized to a high degree [see Supplement 1, Fig. S5(b)]. If this emission is coupled to the spin-locking cavity mode, a σ_+ polarized quantum emitter sitting at the outer sidewall couples to the fundamental TE mode that is circulating in the ring resonator unidirectionally. Due to the opposite transverse spins associated with the inner and outer sidewalls of the ring resonator, emission efficiently extracted by the scatterers sitting at the inner sidewall becomes dominant by the σ-polarized component. This polarization-conversion effect due to the underlying spin–orbit locking leads to a lower polarization degree χ_{PL} for the coupled quantum emitter. Figure 3(d) shows that when the quantum emitter is spectrally on resonance with the cavity, the measured χ_{PL} is strongly reduced to 59%. This is a direct indication of the polarization-conversion effect due to coupling between the quantum emitter and the ring resonator.

We note that the measurement configuration for the experiment in Fig. 3(d) excites and collects directly on top of the quantum emitter, and thus one cannot distinguish between the emission from the cavity mode diffracted from the scatterers at the inner sidewall and the direct PL emission from the emitter itself due to the high NA of the objective. To be able to resolve the polarization states from the emitter and cavity separately, one can investigate the spatial far-field profile of the emission. To this end, we use an EM-CCD imaging camera to record the image-plane and the far-field intensity distributions of the emission and resolve them in σ_+ and σ_- polarization, respectively, as shown in Figs. 4(a) and 4(b). Under the σ_+ detection configuration, one can observe emission to occur only at the location of the emitter, whereas under the σ_- detection, one can see quantum light emission scattered along the entire ring resonator. The fringes along the ring resonator are a result of the interference at the scatterers between the direct emission from the quantum emitter and scattered cavity mode (see Supplement 1, Section S7). To confirm this, we carried out an FDTD simulation for a σ_+ polarized point source located at the edge of the outer sidewall of the ring resonator and placed a field monitor located above the ring resonator to simulate light collected by the objective lens. The computed intensity maps are resolved in σ_+ and σ_- polarization and shown in Figs. 4(d) and 4(e), respectively. The theory confirms the experimentally observed polarization-conversion behavior: the σ_+ polarized point source couples to the cavity mode and light scattered from the cavity is σ_- polarized, while the interference fringes along the ring resonator show a pattern with comparable periodicity. Furthermore, the observed periodicity of this emitter-mode interference is significantly different from the standing mode pattern of the high-order whispering gallery mode of the bare resonator alone (see Supplement 1, Fig. S1c). Note that this interference pattern

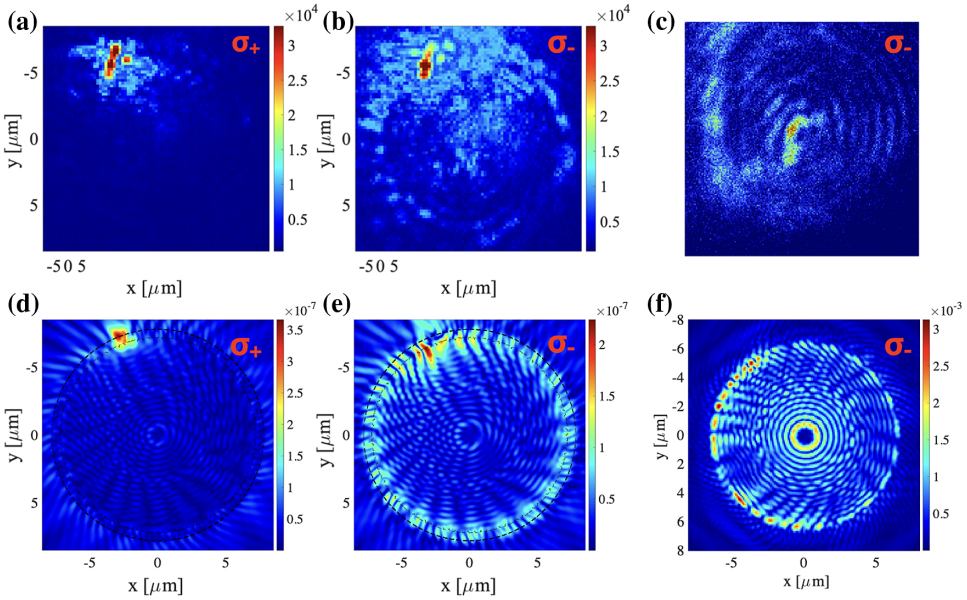

Fig. 4. Far-field imaging of the chiral single photon emission under resonance conditions (a) and (b): Measured image plane pattern with (a) spin-up and (b) spin-down polarization filtering. (c) The measured far-field pattern (Fourier-plane) with spin-down polarization filtering. (d) and (e) show the spin-up and spin-down components, respectively, of the FDTD simulated image plane pattern. (f) The spin-down component of the FDTD simulated far-field pattern.

only occurs in the experiment if the point source is coupled to the cavity mode, which further manifests the coupling effects between the quantum emitter and the ring resonator. In fact, by scanning individual quantum emitters in and out of spectral resonance and observing the far-field image along the ring resonator one can conveniently distinguish quantum emitters that are spatially coupled (interference pattern occurs) or not coupled (no interference pattern occurs), making this technique an interesting alternative to the Purcell effect lifetime measurements discussed in Fig. 3(b).

With circular gratings possessing cylindrical symmetry, light emitted from the WGM forms a Bessel beam after collimation, in contrast to the circular-polarized emission pattern of a bare quantum emitter. To observe the Bessel beam, we filtered out the spin down-polarized component and measured the far-field emission pattern with the imaging camera placed at the Fourier plane. Figure 4(c) shows a Bessel mode pattern with a dark spot at the center and a strong redistribution of the light emission into the left region of the far field. This redistributed quantum light emission is caused by the direct in-plane emission of the quantum emitters further scattered out by the sidewall of the cavity, for the same reason as introduced in Fig. 4(b). To further confirm the Bessel beam far field of the cavity emission, we plot the numerical far-field pattern in Fig. 4(f) by taking the Fourier transform on Fig. 4(e). The far-field pattern shows a similar intensity distribution as compared to Fig. 4(c), proving the chiral single-photon Bessel beam emission with polarization conversion, and thus the coupling between the quantum emitter and the cavity via the underlying spin–orbit locking effect.

3. CONCLUSIONS

In summary, we have demonstrated chiral single-photon emission from microring resonators through spin–orbit locking of strain-induced WSe_2 quantum emitters residing at the outer sidewall. The cavity-coupled quantum emitter shows a pronounced Purcell effect with a lifetime reduction from 5.2 to 3.55 ns when tuned into resonance. The coupled single-photon cavity mode is further extracted to free space via engineered scatterers at the inner sidewall, forming a single-photon Bessel mode with a resulting polarization orthogonal to that of the bare quantum emitter. The demonstrated chiral coupling of spatially deterministic quantum emitters in 2D materials to optical ring resonators enables applications in quantum technology, including spin-photon interfaces for on-chip quantum information processing and chirality-based quantum key distribution. While this work is limited to magnetic field tuning via external superconducting magnets to achieve the spin–orbit locking from quantum confined excitons, we note that recent advances utilizing on-chip magnetic proximity coupling [35,36] as well as electrical voltage-tuning of the ferromagnetic field strength in van der Waals materials [37,38] allows a priory to miniaturize such quantum systems in future work to be integrated fully on-chip. To further increase the Purcell effect, plasmonic nanocavities provide a promising approach to enhance the optical emission by 3 orders of magnitude [39] and push the quantum emitter's lifetime into the coherence (indistinguishability) regime [40]. Ultimately, it would be interesting to create hybrid devices embedding plasmonic gap mode cavities with deterministically coupled QEs directly into the mode maximum of these patterned SiN ring resonators that provide spin–orbit locking, which allows for efficient on-chip OAM state creation and manipulation.

Funding. National Science Foundation (DMR-1420634, ECCS-1932803, ECCS-MRI-1531237, ECCS-Raise-EQuIP-1842612, NNCI-1542153).

Acknowledgment. S.S. acknowledges financial support for the attodry1100 under NSF. S.S. and L.F. acknowledge financial support from the Raise-EQuIP program at NSF. L.F. also acknowledges financial support from the EPMD program at NSF and for a Sloan Research Fellowship. Fabrication work was carried out in part at the Singh Center for Nanotechnology, which is supported by the NSF National Nanotechnology Coordinated Infrastructure. Materials synthesis was supported by the NSF MRSEC program through Columbia in the Center for Precision Assembly of Superstratic and Superatomic Solids.

Disclosures. The authors declare no conflicts of interest.

Data availability. Data underlying the results presented in this paper are not publicly available at this time but may be obtained from the authors upon reasonable request.

Supplemental document. See Supplement 1 for supporting content.

†These authors contributed equally to this paper.

REFERENCES

1. M. A. Nielsen and I. L. Chuang, *Quantum Computation and Quantum Information*, 10th anniversary ed. (Cambridge University, 2010).
2. J. L. O'Brien, "Optical quantum computing," Science **318**, 1567–1570 (2007).
3. K. Y. Bliokh, F. J. Rodríguez-Fortuño, F. Nori, and A. V. Zayats, "Spin–orbit interactions of light," Nat. Photonics **9**, 796–808 (2015).
4. A. M. Yao and M. J. Padgett, "Orbital angular momentum: origins, behavior and applications," Adv. Opt. Photon. **3**, 161–204 (2011).
5. S. Murakami, N. Nagaosa, and S.-C. Zhang, "Dissipationless quantum spin current at room temperature," Science **301**, 1348–1351 (2003).
6. M. Onoda, S. Murakami, and N. Nagaosa, "Hall effect of light," Phys. Rev. Lett. **93**, 083901 (2004).
7. K. Y. Bliokh and Y. P. Bliokh, "Conservation of angular momentum, transverse shift, and spin Hall effect in reflection and refraction of an electromagnetic wave packet," Phys. Rev. Lett. **96**, 073903 (2006).
8. O. Hosten and P. Kwiat, "Observation of the spin Hall effect of light via weak measurements," Science **319**, 787–790 (2008).
9. X. Zhou, Z. Xiao, H. Luo, and S. Wen, "Experimental observation of the spin Hall effect of light on a nanometal film via weak measurements," Phys. Rev. A **85**, 043809 (2012).
10. K. Y. Bliokh, "Geometrical optics of beams with vortices: Berry phase and orbital angular momentum Hall effect," Phys. Rev. Lett. **97**, 043901 (2006).
11. J. Zhu, Y. Chen, Y. Zhang, X. Cai, and S. Yu, "Spin and orbital angular momentum and their conversion in cylindrical vector vortices," Opt. Lett. **39**, 4435–4438 (2014).
12. P. Miao, Z. Zhang, J. Sun, W. Walasik, S. Longhi, N. M. Litchinitser, and L. Feng, "Orbital angular momentum microlaser," Science **353**, 464–467 (2016).
13. V. Garbin, G. Volpe, E. Ferrari, M. Versluis, D. Cojoc, and D. Petrov, "Mie scattering distinguishes the topological charge of an optical vortex: a homage to Gustav Mie," New J. Phys. **11**, 013046 (2009).
14. Z. Zhang, X. Qiao, B. Midya, K. Liu, J. Sun, T. Wu, W. Liu, R. Agarwal, J. M. Jornet, S. Longhi, N. M. Litchinitser, and L. Feng, "Tunable topological charge vortex microlaser," Science **368**, 760–763 (2020).
15. F. J. Rodríguez-Fortuño, G. Marino, P. Ginzburg, D. O'Connor, A. Martínez, G. A. Wurtz, and A. V. Zayats, "Near-field interference for the unidirectional excitation of electromagnetic guided modes," Science **340**, 328–330 (2013).
16. J. Petersen, J. Volz, and A. Rauschenbeutel, "Chiral nanophotonic waveguide interface based on spin-orbit interaction of light," Science **346**, 67–71 (2014).
17. Y. Lefier and T. Grosjean, "Unidirectional sub-diffraction waveguiding based on optical spin–orbit coupling in subwavelength plasmonic waveguides," Opt. Lett. **40**, 2890–2893 (2015).
18. T. V. Mechelen and Z. Jacob, "Universal spin-momentum locking of evanescent waves," Optica **3**, 118–126 (2016).
19. P. Lodahl, S. Mahmoodian, S. Stobbe, A. Rauschenbeutel, P. Schneeweiss, J. Volz, H. Pichler, and P. Zoller, "Chiral quantum optics," Nature **541**, 473–480 (2017).
20. Z. Shao, J. Zhu, Y. Chen, Y. Zhang, and S. Yu, "Spin-orbit interaction of light induced by transverse spin angular momentum engineering," Nat. Commun. **9**, 926 (2018).
21. B. Chen, Y. Wei, T. Zhao, S. Liu, R. Su, B. Yao, Y. Yu, J. Liu, and X. Wang, "Bright solid-state sources for single photons with orbital angular momentum," Nat. Nanotechnol. **16**, 302–307 (2021).
22. R. J. Coles, D. M. Price, J. E. Dixon, B. Royall, E. Clarke, P. Kok, M. S. Skolnick, A. M. Fox, and M. N. Makhonin, "Chirality of nanophotonic waveguide with embedded quantum emitter for unidirectional spin transfer," Nat. Commun. **7**, 11183 (2016).
23. C. Javerzac-Galy, A. Kumar, R. D. Schilling, N. Piro, S. Khorasani, M. Barbone, I. Goykhman, J. B. Khurgin, A. C. Ferrari, and T. J. Kippenberg, "Excitonic emission of monolayer semiconductors near-field coupled to high-Qmicroresonators," Nano Lett. **18**, 3138–3146 (2018).
24. D. Rosser, T. Fryett, A. Ryou, A. Saxena, and A. Majumdar, "Exciton–phonon interactions in nanocavity-integrated monolayer transition metal dichalcogenides," NPJ 2D Mater. Appl. **4**, 20 (2020).
25. C. Palacios-Berraquero, D. M. Kara, A. R.-P. Montblanch, M. Barbone, P. Latawiec, D. Yoon, A. K. Ott, M. Loncar, A. C. Ferrari, and M. Atatüre, "Large-scale quantum-emitter arrays in atomically thin semiconductors," Nat. Commun. **8**, 15093 (2017).
26. A. Branny, S. Kumar, R. Proux, and B. D. Gerardot, "Deterministic strain-induced arrays of quantum emitters in a two-dimensional semiconductor," Nat. Commun. **8**, 15053 (2017).
27. Y. Luo, G. D. Shepard, J. V. Ardelean, D. A. Rhodes, B. Kim, K. Barmak, J. C. Hone, and S. Strauf, "Deterministic coupling of site-controlled quantum emitters in monolayer WSe_2 to plasmonic nanocavities," Nat. Nanotechnol. **13**, 1137–1142 (2018).
28. F. Peyskens, C. Chakraborty, M. Muneeb, D. Van Thourhout, and D. Englund, "Integration of single photon emitters in 2D layered materials with a silicon nitride photonic chip," Nat. Commun. **10**, 4435 (2019).
29. Z. Ye, D. Sun, and T. F. Heinz, "Optical manipulation of valley pseudospin," Nat. Phys. **13**, 26–29 (2017).
30. Y. Luo, N. Liu, B. Kim, J. Hone, and S. Strauf, "Exciton dipole orientation of strain-induced quantum emitters in WSe_2," Nano Lett. **20**, 5119–5126 (2020).
31. K. Y. Bliokh and F. Nori, "Transverse and longitudinal angular momenta of light," Phys. Rep. **592**, 1–38 (2015).
32. X. Li, G. D. Shepard, A. Cupo, N. Camporeale, K. Shayan, Y. Luo, V. Meunier, and S. Strauf, "Nonmagnetic quantum emitters in boron nitride with ultranarrow and sideband-free emission spectra," ACS Nano **11**, 6652–6660 (2017).
33. S. Kumar, A. Kaczmarczyk, and B. D. Gerardot, "Strain-induced spatial and spectral isolation of quantum emitters in mono- and bilayer WSe_2," Nano Lett. **15**, 7567–7573 (2015).
34. Q. Wang, J. Maisch, F. Tang, D. Zhao, S. Yang, R. Joos, S. L. Portalupi, P. Michler, and J. H. Smet, "Highly polarized single photons from strain-induced quasi-1D localized excitons in WSe_2," Nano Lett. **21**, 7175–7182 (2021).
35. K. Shayan, N. Liu, A. Cupo, Y. Ma, Y. Luo, V. Meunier, and S. Strauf, "Magnetic proximity coupling of quantum emitters in WSe_2 to van der Waals ferromagnets," Nano Lett. **19**, 7301–7308 (2019).
36. N. Liu, C. M. Gallaro, K. Shayan, A. Mukherjee, B. Kim, J. Hone, N. Vamivakas, and S. Strauf, "Antiferromagnetic proximity coupling between semiconductor quantum emitters in WSe_2 and van der Waals ferromagnets," Nanoscale **13**, 832–841 (2021).
37. B. Huang, G. Clark, D. R. Klein, D. MacNeill, E. Navarro-Moratalla, K. L. Seyler, N. Wilson, M. A. McGuire, D. H. Cobden, D. Xiao, W. Yao, P. Jarillo-Herrero, and X. Xu, "Electrical control of 2D magnetism in bilayer CrI_3," Nat. Nanotechnol. **13**, 544–548 (2018).
38. X. Wang, J. Tang, X. Xia, C. He, J. Zhang, Y. Liu, C. Wan, C. Fang, C. Guo, W. Yang, Y. Guang, X. Zhang, H. Xu, J. Wei, M. Liao, X. Lu, J. Feng, X. Li, Y. Peng, H. Wei, R. Yang, D. Shi, X. Zhang, Z. Han, Z. Zhang, G. Zhang, G. Yo, and X. Han, "Current-driven magnetization switching in a van der Waals ferromagnet Fe_3GeTe_2," Sci. Adv. **5**, eaaw8904 (2019).
39. G. M. Akselrod, C. Argyropoulos, T. B. Hoang, C. Ciracì, C. Fang, J. Huang, D. R. Smith, and M. H. Mikkelsen, "Probing the mechanisms of large Purcell enhancement in plasmonic nanoantennas," Nat. Photonics **8**, 835–840 (2014).
40. Y. Luo, X. He, Y. Kim, J. L. Blackburn, S. K. Doorn, H. Htoon, and S. Strauf, "Carbon nanotube color centers in plasmonic nanocavities: a path to photon indistinguishability at telecom bands," Nano Lett. **19**, 9037–9044 (2019).